

Optimum optical designs for diffraction-limited terahertz spectroscopy and imaging systems using off-axis parabolic mirrors

Nishtha Chopra · James Lloyd-Hughes

Received: date / Accepted: date

Abstract Off-axis parabolic mirrors (OAPMs) are widely used in the THz and mm-wave communities for spectroscopy and imaging applications, as a result of their broadband, low-loss operation and high numerical apertures. However, the aspherical shape of an OAPM creates significant geometric aberrations that make achieving diffraction-limited performance a challenge, and which lowers the peak electric field strength in the focal plane. Here we quantify the impact of geometric aberrations on the performance of the most widely-used spectrometer designs, by investigating whether diffraction-limited performance can be achieved in both the sample and the detector plane. We identify simple rules, based on marginal ray propagation, that allow spectrometers to be designed that are more robust to misalignment errors, and which have minimal aberrations for THz beams. For a given source this allows the design of optical paths that give the smallest THz beam focal spot, with the highest THz electric field strength possible. This is desirable for improved THz imaging, for better signal-to-noise ratios in linear THz spectroscopy and optical-pump THz-probe spectroscopy, and to achieve higher electric field strengths in non-linear THz spectroscopy.

Keywords Terahertz · off-axis parabolic mirror · ray tracing

1 Introduction

Within the research community, different optical setups containing off-axis parabolic mirrors (OAPMs) are widely utilized to characterise broadband THz radiation sources [1–3], as well as to perform linear THz spectroscopy in the transmission or reflection geometry [4, 5], non-linear THz spectroscopy [6], optical-pump THz-probe spectroscopy (OPTPS) [7] and near-field THz microscopy [8]. The optimum performance for a THz spectrometer will be achieved if an aberration-free image of the THz source can be formed at each focal plane. For linear THz spectroscopy, a minimal spot size is often desired: to investigate samples that are small in transverse extent [9]; to couple more effectively to sub-wavelength structures and waveguides [10]; or to image spatially inhomogeneous materials, such as large-area graphene [11]. Further, the signal detected in the detector plane (*e.g.* via electro-optic sampling or photoconductive detection) in THz time-domain spectroscopy is proportional to the electric field of the THz beam (rather than the area- and time-integrated power, as in a bolometer or pyroelectric), and is hence larger when the THz beam has a smaller area. In OPTPS, the THz probe beam must have a smaller spatial extent than the optical pump beam, in order to probe a uniform carrier density: it is therefore also desirable to have a smaller THz beam so this condition can be readily achieved for lower power optical pump lasers [12]. Finally, intense THz pulses with high electric field strengths (typically > 100 kV/cm) can be used to study the non-linear dynamical motion of vibrational modes or free charges [6]. For non-linear THz spectroscopy, it is thus important to efficiently focus one or more THz beams down to as close to the diffraction limit as possible, to obtain the highest electric field strength.

The majority of sources of broadband THz radiation (such as photoconductive antennae, optical rectification in non-linear crystals and spintronic emitters) produce THz beams that propagate in free space in the fundamental (TEM_{00}) transverse Gaussian mode. The Gaussian nature of terahertz (THz) beams has been corroborated through a combination of theoretical and experimental techniques, wherein, scalar and vectorial diffraction theory has been

N. Chopra
Department of Physics, University of Warwick, Coventry, United Kingdom E-mail: nishtha.chopra@warwick.ac.uk

J. Lloyd-Hughes
Department of Physics, University of Warwick, Coventry, United Kingdom E-mail: j.lloyd-hughes@warwick.ac.uk

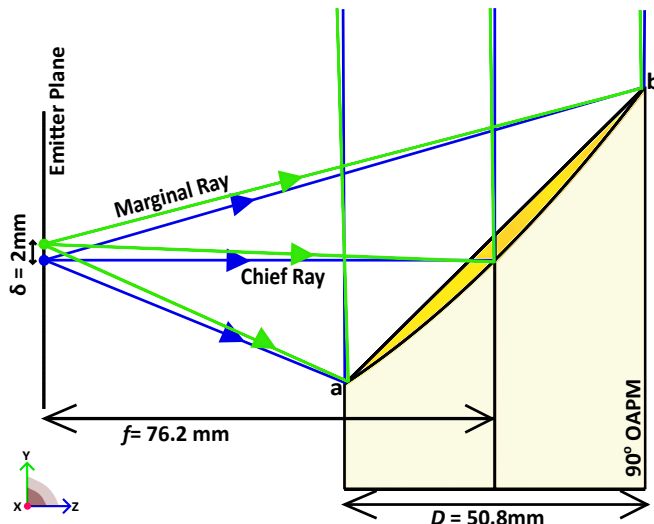


Fig. 1: Geometry of a right-angle OAPM.

utilized to analyze the far-field behaviour of the THz pulses [13]. Similarly, experimental validation was achieved by imaging the spatial and temporal distribution of pulses, in a standard THz-TDS setup [14]. In free space, the divergence angle of this Gaussian mode is $\theta = \lambda/\pi w_0$ in the paraxial approximation, where w_0 is the radius of the initial beam waist. For example, $\theta = 18^\circ$ for light at 1 THz ($\lambda = 300 \mu\text{m}$) for $w_0 = 300 \mu\text{m}$, and the divergence angle increases for longer wavelengths or smaller initial beam sizes. Hence, THz radiation tends to diverge rapidly, and large numerical aperture optics are required, in particular, to collect low-frequency components with longer wavelengths [15]. While polymer lenses are widely adopted in many THz systems due to their light weight and ease of fabrication [4], their finite Fresnel losses and absorption reduces optical throughput, and they can introduce optical aberrations.

To overcome these challenges, high-reflectivity metal-coated off-axis parabolic mirrors (OAPMs) are widely used [15]. An OAPM is a segment of a parent parabolic surface and can be defined by the off-axis angle, reflected effective focal length f and diameter D , as illustrated in Fig. 1. These mirrors offer broadband performance while eliminating Fresnel losses, and can collimate a beam diverging from an on-axis point source without aberrations, or focus a collimated beam to a diffraction-limited spot. In the geometric optics (ray optics) picture, an OAPM can perfectly collimate rays of light that originate from a point source only if the point source is on the optical axis and in the focal plane, at a distance f from the mirror (blue rays in Fig. 1). However, real THz sources have a finite spatial extent, set by the size of the incident laser beam or the emitter's active area in laser-based THz systems, and the propagation of light from off-axis points in the object plane must also be considered (green rays in Fig. 1).

Different optical analysis techniques have been deployed to model OAPM systems, such as deriving analytical expressions for Hermite-Gaussian beam propagation after reflection from an OAPM in the paraxial approximation [16] or by using optical ray tracing methods [17, 18]. In the former case, after a fundamental Gaussian beam was incident onto an OAPM, the reflected electric field was found to have a skewed and broadened profile corresponding to the presence of additional higher order (TEM_{30} and TEM_{12}) Hermite-Gaussian modes [16]. Importantly, by adding a second OAPM placed at the correct distance and with the right orientation, it was shown that the distortions introduced by the second mirror can cancel out the distortions introduced by the first mirror, resulting again in a clean fundamental Gaussian beam (desirable in order to achieve a diffraction-limited spot). Alternatively, analytical ray tracing was used to show that if a collimated beam of light is incident onto an OAPM at an angle away from its optical axis, the focal spot is distorted [17].

While analytical approaches are useful for specific cases where the underlying assumptions are valid, they become cumbersome for realistic optical systems containing many OAPMs. An alternative approach is to use ray tracing software, in which point sources can be readily placed at different positions to assess the optical performance for objects with finite extent, or for point sources that are placed off-axis. Further, an arbitrary number of optical components can be included. Brückner *et al.* used the ZEMAX ray tracing software to show that for an off-axis point source, the beam after a single right-angled OAPM has an astigmatic wavefront [18]. Further, and similar to the conclusion derived in Murphy's work using analytical theory [16], Brückner *et al.* demonstrated that a judiciously-oriented second OAPM can cancel out the astigmatic wavefront, leading to diffraction-limited performance for off-axis field points. It was shown that the second OAPM, which was placed in a $4f$ geometry, has to be oriented to send the reflected beam anti-parallel to the original beam direction (i.e. along $-z$ if the THz

source radiates along z) in order to substantially cancel out aberrations for off-axis field points. This was in contrast to the alternative orientation for the second OAPM, reflecting the THz beam along $+z$, in which aberrations were evident.

Based on these considerations, Laurita *et al.* subsequently performed an experimental comparison of the two geometries and showed that the beam waist at the sample focus of a typical THz-TDS system was smaller, at around 7 mm compared to 11 mm, for the aberration-corrected arrangement than the alternative orientation [19]. However, diffraction-limited performance was not achieved and the performance of the different OAPM arrangements in the detector plane was not considered. Recently, the present authors experimentally investigated a linear array of photoconductive THz emitters, where each pixel acted as a THz source at a different distance from the optical axis [3], and reported close to the diffraction-limited performance obtained using an arrangement of OAPMs that corrected for aberrations.

Given the above challenges for optical systems containing OAPMs, it is timely and pertinent to consider how best to minimise geometric aberrations, such that diffraction-limited performance can be achieved at both the sample position and the detector position in THz spectrometers. In this Article, we provide a comprehensive analysis of how the design of a spectrometer impacts its performance, with particular emphasis on the spatial and temporal spread in the sample and detector focal planes. In Section 2 we describe the modelling approach taken: we used the ZEMAX optical design software to ray trace the beam path for the two optical systems most commonly used in THz spectroscopy, as well as an uncommon but optimum design, starting from a variety of on- and off-axis points. Further, we introduce a notation that captures the relative orientation of different OAPMs based on marginal ray propagation. We then, in Section 3, examine and evaluate the performance of the different spectrometer designs by using spatial plots of ray propagation, and optical path differences in the time-domain. In Section 4 we conclude our analysis by ranking the three competing optical designs in terms of their robustness to misalignment, and their ability to form accurate images of the THz source in the sample plane and the detector plane. Finally, we use the insights gained from ray tracing and marginal ray propagation to predict the optimum arrangement of OAPMs for a reflection geometry setup.

2 Modelling approach and spectrometer designs

In this Section we define the ray-tracing methodology used and describe the key nomenclature used in the optical design field. Illustrated in Fig. 1 is a right-angled mirror viewed in the $y-z$ plane, also termed the tangential plane. The $x-z$ plane is referred to as the sagittal plane. The ray that propagates from the focus in the emitter plane along z , along the optical axis of the OAPM, is referred to as the *chief ray*: it changes direction by 90° after hitting the geometric centre of the OAPM, to travel along y . *Marginal rays* are incident on the edges of the OAPM, and span the maximum aperture as seen from the geometric centre. The asymmetric shape of the OAPM is particularly evident when considering the two marginal rays that hit the closest side (at point a) or the furthest side (point b) of the OAPM, as the two marginal rays travel at different angles to the chief ray. Here, all OAPMs were assumed to be right-angled, with $f = 76.2$ mm and $D = 50.8$ mm, representative of the mirrors most often used. For this choice, the numerical aperture was 0.31, and the angle of the marginal rays to the chief ray was $\alpha \simeq \tan^{-1}(D/2f) = 18.4^\circ$. This is similar to the divergence calculated above for a 1 THz Gaussian beam, suggesting that the majority of the THz radiation produced by the emitter would be collected by this OAPM, and that the OAPM would be filled effectively such that smaller diffraction-limited beam foci can be achieved.

Typical THz spectroscopy and imaging systems require at least two pairs of two OAPMs: the first pair collects the THz radiation from the source, and focuses it onto a sample, while the second pair collects the transmitted or reflected THz beam and focuses it onto a detector. There are a substantial number of degrees of freedom possible for a complete spectrometer design, as each individual OAPM has six positional degrees of freedom (three translational and three rotational). Here we examined the most common spectrometer designs, which consist of four right-angled OAPMs, with their optical axes all within the same plane (here denoted $y-z$). For each OAPM added to an optical setup there are two options for its orientation that keep the optical axis in the same plane: these change the beam direction by $\pm 90^\circ$ relative to its previous direction in the $y-z$ plane.

To describe three different geometries reported in the literature we define the nomenclature U-shape, step-shape and S-shape to refer to the spectrometers illustrated in Figs. 2(a)-(c), based on the pattern formed when considering the chief ray's beam path (yellow lines and arrows). The U-shape and step-shape design are the most widely used in THz time-domain spectrometers, while the S-shape was suggested to minimise aberrations in the sample plane [19]. Laurita *et al.* compared the performance of the U-shape and S-shape (referred to as the "conventional" and "modified" designs in their work), but did not consider the step-shape or the performance in the detector plane. In the U-shape and step-shape designs [Figs. 2(a)-(b)], the first two OAPMs are oriented identically, but the designs differ in how the second pair of OAPMs is oriented. For the U-shape, the second pair of OAPMs is oriented to

return the THz beam to the same y co-ordinate, leading to a relatively compact design, while the step- and S-shapes have a larger size in y .

We stress here that the U-shape does not have the correct layout to collect all the *on-axis* rays after the second OAPM: across the sample plane, the marginal rays highlighted in red are *not* collected by the third OAPM [Figs. 2(a)], and hence the throughput of the system is not perfect. This problem is not seen for the step-shape or S-shape, where the third OAPMs are oriented correctly, and all the marginal rays after the sample plane are collected.

Based on a consideration of the marginal rays and the symmetry properties of an OAPM system, we define here a nomenclature that we find useful to describe the optical arrangement of pairs of OAPMs, inspired by the Glazer and Aleksandrov notation schemes widely used to describe the tilt patterns of perovskite octahedra. As we show in the following section, the orientation of each OAPM within a pair and the relative orientation of each pair of OAPMs are both critical to achieve minimal aberrations. Therefore, we introduce the notation (x_i, x_j) to denote the orientation of a pair of OAPMs, where $x = a, b$ to denote whether or not the marginal ray reflects from the “near” side or “far” side points a and b in Fig. 1, and the subscript denotes the focal lengths f_i and f_j . If the focal lengths of all mirrors are identical, as in this work, we drop the subscript notation. With this scheme, the U-shape design can be written $(a, b)(a, b)$ as pictured by the cyan ray in Fig. 1(a), as the marginal ray that reflects from point a on the first OAPM then reflects from b, a and b points on the subsequent mirrors. The step-shape can be written $(a, b)(b, a)$ and the S-shape is $(a, a)(a, a)$. Retaining the brackets is useful as a guide to show where the foci of the optical system are, namely before and after each bracket.

To assess the performance of each setup, we introduced an offset in the position of the point source in the emitter (object) plane, either in the y -direction, as illustrated in Fig. 1, in the x direction, or in both. As a consequence of the point source being off-axis by a distance $\delta = 2$ mm, rays propagate at a slight angle 1.5° after the first OAPM, in comparison to the on-axis rays. This tilt can be observed in Fig. 2(d), where the off-axis rays are represented in green. The second OAPM, which forms an (a, b) orientation pair, focused rays to a point at a distance $-\delta$ in y

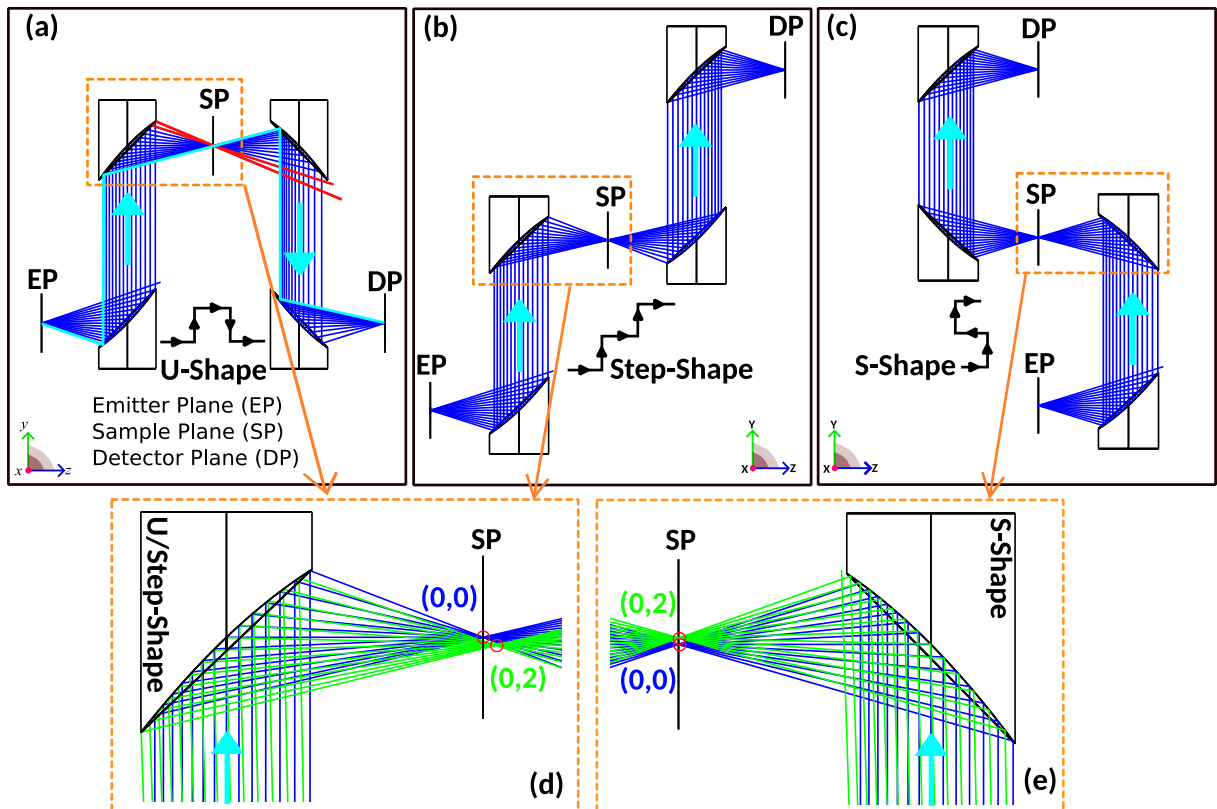


Fig. 2: Ray tracing models of three different THz-TDS geometries for an on-axis point source at centred at $(0, 0)$ in the emitter plane (EP), propagating to the sample plane (SP) and detector plane (DP). (a) U-geometry, or $(a, b)(a, b)$ using the notation defined in the text. The red highlighted marginal rays are not captured as they propagate. (b) Step-geometry, or $(a, b)(b, a)$ arrangement. The second OAPM pair is oriented the same as the first. (c) S-geometry, or $(a, a)(a, a)$ setup. (d) For the U- and step-shapes, propagation from an off-axis $(0, 2)$ source, shown as green rays, leads to a tangential plane focus behind the SP focus for on-axis propagation, thus creating aberrations. (e) For the sample plane of the S-geometry, the off-axis rays rays from $(0, 2)$ converge in the SP with minimal aberration.

from the optical axis, where the negative sign signifies that the image formed after the two OAPMs was inverted, and at a distance along the z axis after from the SP. In the sagittal plane (not shown here) the focus forms before the SP. Notably, for the alternative orientation of the second OAPM, (a, a) , pictured in Fig. 2(e), the off-axis rays are refocussed at the SP. In order to better investigate the impact of OAPM orientation we now consider the spatial and temporal performance of the different designs in more detail.

3 Results

In a ray-traced model of an optical system, whether or not an optical system can achieve diffraction-limited performance can be assessed by examining “spot diagrams,” which show the spatial distribution of rays as they intersect the focal plane, and comparing it to the diffraction-limited beam size, for instance, given by an Airy disk. Alternatively, because ray tracing keeps track of the phase of the electric field, the optical path difference (OPD) of different rays can be determined relative to the chief ray. The system can be assumed to be diffraction limited if the phase change for all rays is sufficiently small: an OPD of less than a quarter wavelength is a common convention used in the optical modelling community to define diffraction-limited performance. To comprehensively assess image quality, we conducted a comparative analysis of the spatial distribution and the temporal evolution of the THz field across all geometries, at a frequency of 1 THz (wavelength $\lambda = 300\mu\text{m}$). Note that the only impact of the wavelength is that it changes the diameter of the diffraction-limited spot size.

3.1 Spatial performance

Spot diagrams provide essential visual indicators to assess the symmetry of aberrations and image quality, and are reported in Fig. 3 for each geometry (three rows) and at both the sample plane (left-hand column) and in the detector plane (right-hand column). In each case, the sequence of spot diagrams shows how the beam propagates through the focus in steps of 1 mm along the beam propagation direction. Different colours represent the spot diagrams obtained for on-axis and off-axis point sources. The spot diagrams are made up of a large number of spots, not all of which are separable on the scale shown here (10 mm by 10 mm for each spot diagram), where 1 mm corresponds to one of the smaller grey squares. It is evident for all geometries that propagation from an on-axis point source (blue points) is well-behaved, in that the rays traverse the system and reach a point-like focus both in the SP and the DP.

Considering the spot diagrams for the SP for the U-shape and the step-shape (top-left and middle-left black rectangles), which are identical owing to sharing the same initial (a, b) geometry, it is clear that a small offset of 2 mm in x or y is sufficient to substantially distort the shape of the beam through the focus. The offset in y (green) creates a beam that is narrowest in x at a defocus of -2 mm along the beam direction, while the narrowest beam width in y lies around a defocus of 2 mm (corresponding to the case shown in Fig. 2(d)). In either case the minimum beam waist is around 2 times the diffraction-limited size at 1 THz, as evident from a comparison with the black circles (Airy disks), which have radius $\phi_r = 1.22\lambda/f_{\#}$ for f-number $f_{\#}$. The system does not have diffraction-limited performance at 1 THz or higher frequencies, as the Airy disk reduces in diameter at higher frequencies.

In contrast, for the S-shaped design, with (a, a) OAPMs, the performance at the sample position (bottom-left) is excellent for all the off-axis points pictured. The reason for the better performance can be intuitively understood as follows: at the second OAPM the marginal rays hit a matched surface, such that the distortion in the wavefront introduced by the first OAPM can be “inverted” by the second OAPM, as the beam propagates to the focus. Considering the (a, a) configuration further, we found it continued to achieve diffraction-limited performance for offsets as large as ± 4 mm, although for larger offsets (*e.g.* 8 mm) the beam tilt in the tangential plane in the collimated section became too substantial and a large fraction of marginal and central rays were lost.

We continue to discuss the spot diagrams in Fig. 3 by considering the right-hand column, which illustrates the spot diagrams close to the detector plane for the same point source offsets and defocus positions as discussed above. From these diagrams, it is clear that the U-shape and step-shape designs have substantially different imaging performances at the detector plane. For the U-shape, the aberrations evident at the SP are further compounded by the second OAPM pair, such that the off-axis spots are even larger in the DP. In contrast, for the step shape geometry, the DP performance is diffraction limited and comparable to that of the S-shape.

3.2 Temporal performance

Spot diagrams offer a purely geometric perspective on aberrations, providing insights into their spatial characteristics. However, for a more comprehensive understanding, it proves advantageous to investigate the optical path

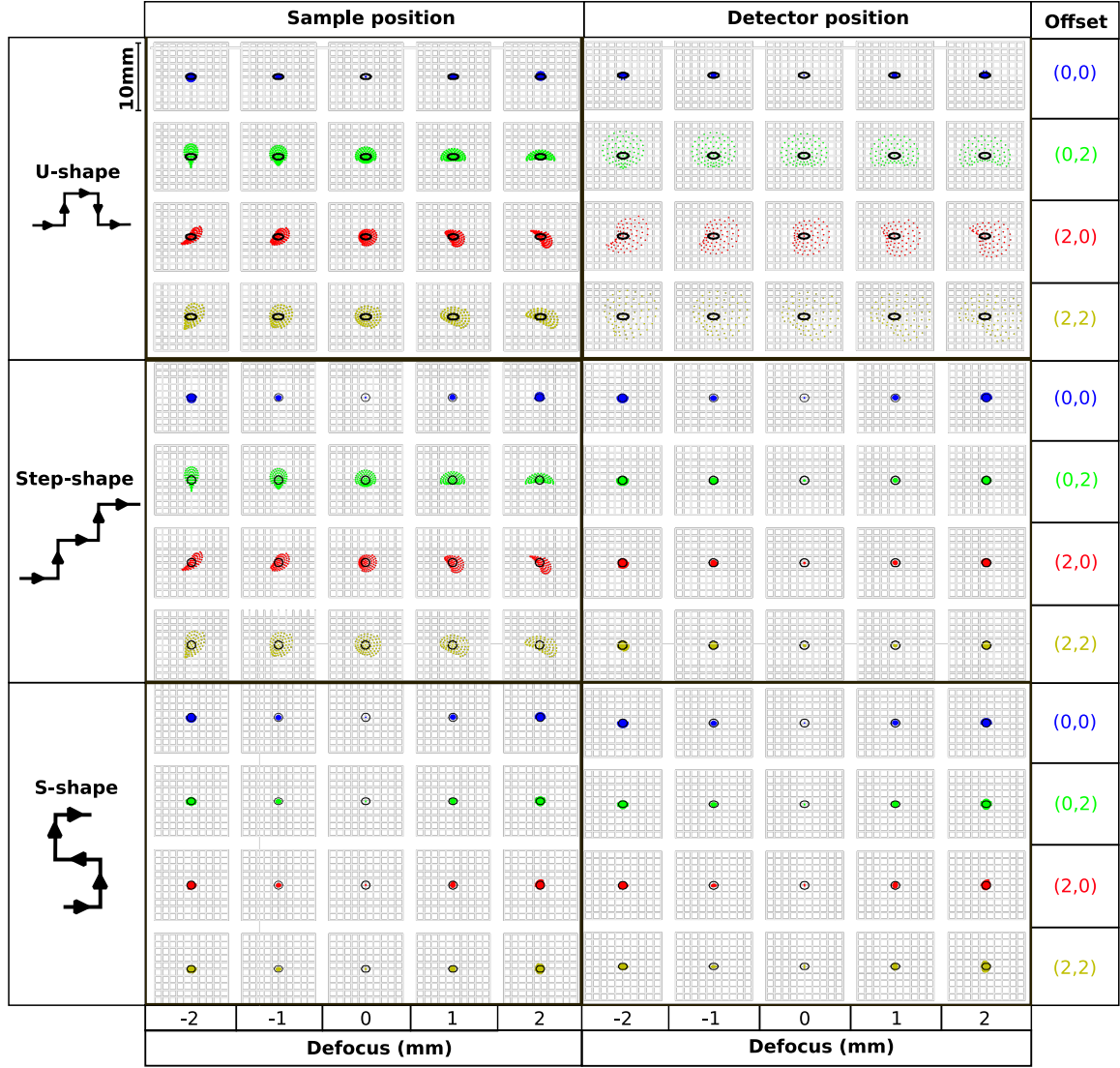


Fig. 3: Spatial profile of the THz beam near the sample plane (left column) and detector plane (right column), for the three different designs (rows). Within each black rectangle, spot diagrams are shown for a particular plane and design, as a function of the offset of the source in the emitter plane and the “defocus” - the difference along z from the ideal focus. The colours and far right-hand labels indicates the (x, y) offsets of the point source in the emitter plane (in mm). Every plot has an Airy-disk (black line) that provides a visual indicator of the diffraction-limited beam size at 1 THz ($\lambda = 300\mu\text{m}$) for an entrance pupil diameter of 50.8 mm. The U-geometry has significant aberrations for a 2 mm offset, both at the SP and at the DP: rays fall outside the Airy disk limit, and the image is distorted. The DP performance of the step-geometry is poor at the SP but good at the DP, while the S-shape rays fall within the Airy disk for both SP and DP, and it exhibits the least aberrations.

difference (OPD) of the system relative to the ideal wavefront surface, taken to be a sphere with radius f , centred at the chief ray’s position in the image plane. The OPD is then calculated for the different rays and is shown graphically by plotting it as a function of the position normalised by the radius of the last optic in the plane of the exit pupil, where P_x and P_y correspond to the exit pupil’s coordinates in the sagittal and tangential planes, respectively. In Figure 4 we present the OPD for the sample plane versus P_x (top row) and P_y (bottom row), for various point source positions in the emitter plane (left to right), and for each design. While the OPD is often shown as the path difference divided by the wavelength, we opted here to show the OPD as a time delay to allow a better understanding of the scale of the OPD changes for the THz time-domain spectroscopy community.

For the on-axis case, $(0,0)$, the horizontal lines in the top-left and bottom-left panels in Fig. 4 signify the absence of an optical path difference (OPD) for all designs, i.e. zero phase difference, representing a perfect spherical wavefront converging to a point image. The off-axis points (representing translational misalignment or finite beam size) result in the incident wavefront converging at the focal point with a slight tilt caused by either the

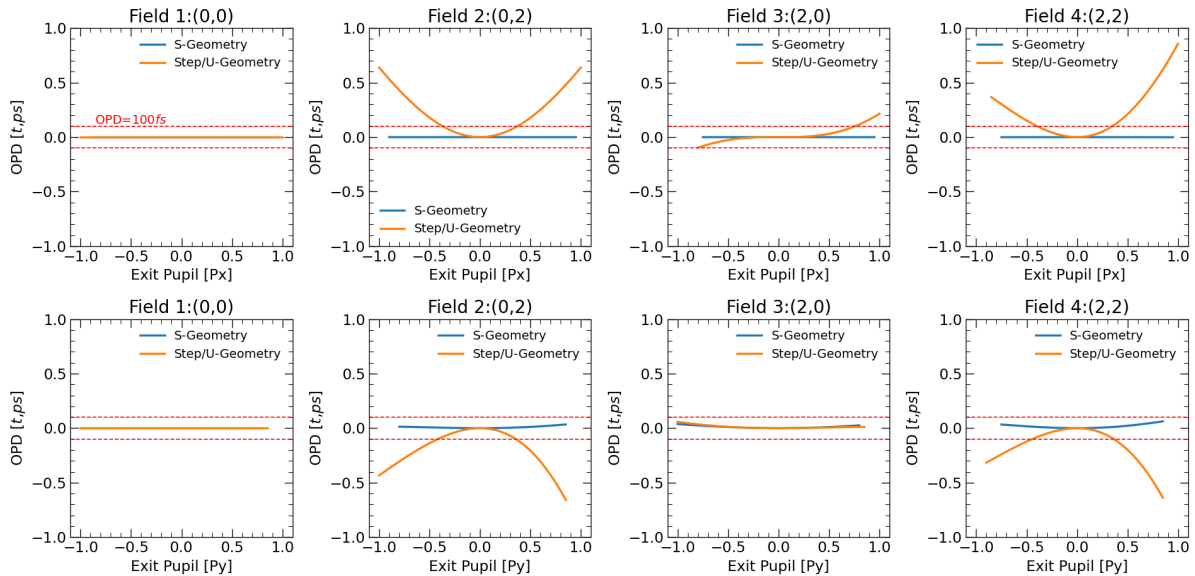


Fig. 4: Wavefront distortion illustrated by the optical path difference for the first two OAPMs. The plot presents the tangential (P_y) and sagittal plane (P_x) optical path differences at the exit pupil. The dashed red line denotes the typical fs laser pulse duration (100 fs) used in THz-TDS setups. The OPD is not defined for exit pupil coordinates where there are no rays on the final OAPM (because of beam tilt), for example along P_y in the S-geometry for (0,2).

delayed or advanced arrival of these rays. For the (0,2) field point a parabola-like OPD can be seen in P_x and P_y for the step and U geometries, with large OPD values > 500 fs for the marginal rays (rays at large positive or negative values of P_x or P_y). In contrast, for S-geometry, the OPD change is small.

For THz time-domain spectroscopy applications, it is important to assess how the different path lengths impact upon the THz pulse duration at the sample position. One could average over the OPD curve by using an assumed profile for the THz beam at the exit pupil (*e.g.* a Gaussian) to weight the amplitude for each ray. Rather than perform that exercise, which would be wavelength and beam specific, we instead highlight the typical pulse duration of the fs laser pulses (~ 100 fs) used in THz time-domain spectroscopy by the horizontal dashed lines. An OPD larger than this limit will introduce a substantial phase shift, and hence will broaden the duration of a THz pulse, simultaneously lowering the peak amplitude of the THz electric field. It is clear from Fig. 4 that for off-axis points (*e.g.* from poor emitter alignment) the temporal duration of the THz pulse at the sample plane is likely to be longer in duration for the step- and U-geometries, as a result of geometric aberrations. Further, it can be seen that precise alignment in the y direction is more critical (the OPDs are smaller for offsets in x).

The OPD for the complete 4 OAPM optical setups is illustrated in Fig. 5, which provides a clear depiction of why the aberrations in the DP differ for the three geometries. The OPD for off-axis point sources is largest for the U-geometry, reaching as large as 1 ps (green curves), suggesting that the U-shape will temporally broaden the THz pulse at the detection position as a result of the substantial geometric aberrations. In comparison, the step-shape (orange curves) and S-geometry (blue curves) have a phase difference near zero, and within the ± 100 fs limit that we suggest is important for typical THz time-domain spectrometer systems.

While the excellent performance of the S-geometry can be assumed to result from the cancellation of distortions within each pair in the $(a,a)(a,a)$ orientation, the similar performance of the step-shape at the detector position, and the poor performance of the U-shape need further explanation. The relative performance can be explained by considering the OPD introduced by each OAPM pair, as well as keeping track of the relative orientation of each pair using the marginal ray notation introduced above: $(a,b)(b,a)$ for the step-shape and $(a,b)(a,b)$ for the U-shape. For the first OAPM pair, the (a,b) orientation creates a distorted wavefront for an off-axis field point, for example, the roughly parabolic OPDs in P_x and P_y seen in Fig. 4 for a (0,2) point source in the emitter plane. In the step-shape, the second OAPM pair has (b,a) orientation, and is in the same orientation in the lab coordinate system as the first pair. However, the OPD that the (b,a) pair produces is not the same as for the first (a,b) pair, because the image is inverted from the EP to the SP: *e.g.* the (0,2) point in the emitter plane maps to (0,-2) in the sample plane. Critically, the OPD flips in sign for inverted field points in the $x-y$ plane [18]. Thus the OPD (or wavefront distortion) created by the second, (b,a) pair in the step-geometry acts to cancel out the OPD of the

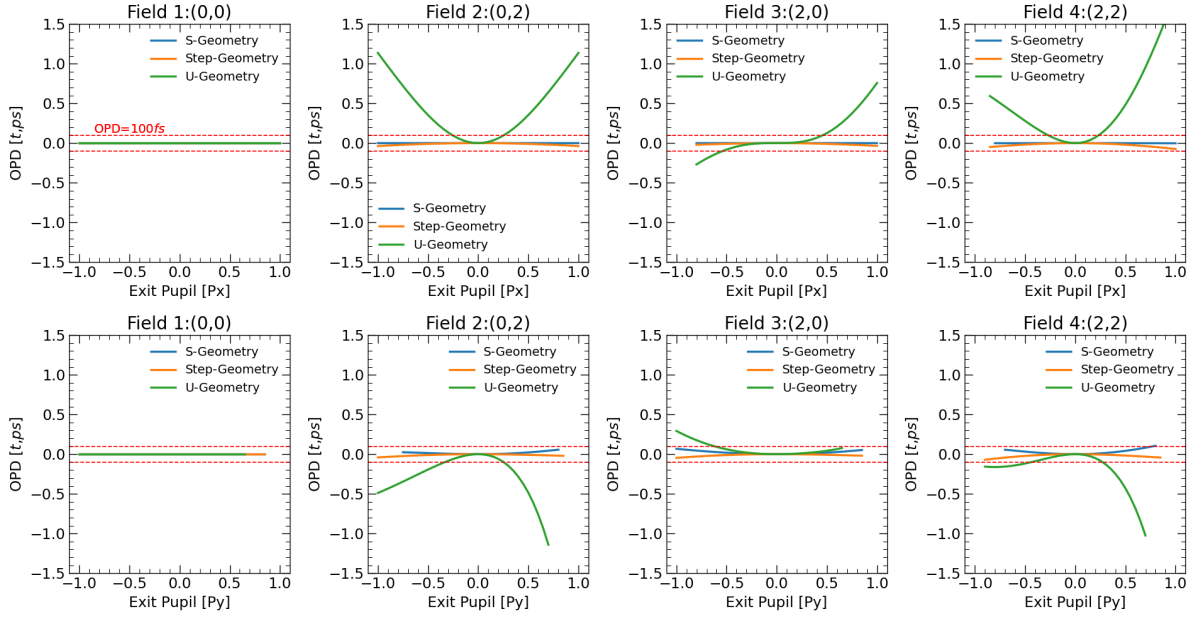


Fig. 5: Wavefront distortion illustrated by the optical path difference for the entire optical path to the detection plane. The S- and step-geometry (blue and orange respectively) demonstrate a superior performance for off-axis points, showing minimal path difference and the least temporal broadening. On the other hand, for the U-geometry, we observe that translational misalignment rapidly cause wavefront aberrations leading to large OPDs.

first pair. In contrast, if the second pair has (a, b) orientation, as in the U-shape, the OPD of the second pair has the same sign, and the wavefront distortions add rather than subtract.

4 Discussion

From the results presented above we can conclude that the S-shape geometry should be adopted in linear, non-linear and OPTP spectroscopy applications, as it is the most robust to the misalignment of the THz source in the $x - y$ plane, and can best cancel out aberrations introduced by the OAPMs in order to achieve a diffraction-limited performance in both the SP and DP. For linear THz spectroscopy, how critical it is to achieve diffraction-limited performance at the intermediate focal plane (the sample position) depends on the application: if raster scanned images are required, or if samples with small $x - y$ extent are studied, then it is clearly advantageous to also work with the S-shape geometry. However, if only spectroscopic measurements are desired, and the highest peak electric field/smallest beam area at the sample position is not critical, then the step-shape can be alternatively used as it has comparable performance to the S-shape in the DP.

While the magnitude of the geometric aberrations in the SP and DP are properties of the spectrometer design and the EP offset, whether or not diffraction-limited performance can be achieved depends on the wavelength and it is therefore useful to consider the frequency-dependent performance of each design. For example, diffraction-limited performance is not achieved at 1 THz in the SP for the U- and step-geometries (Fig. 3) for a 2 mm offset, because geometric aberrations cause rays to fall over a region about twice the diameter of the Airy disk. However at 500 GHz, where the Airy disk doubles in radius relative to that at 1 THz, the majority of rays would fall within the Airy disk and diffraction-limited performance would be achieved at the SP. For higher THz frequencies, the Airy disk reduces in diameter and the relative contribution of aberrations becomes more significant.

Based on a consideration of the spot diagrams and OPDs presented above, we can now suggest rules to aid the design of OAPM systems for THz spectroscopy and imaging:

1. geometric aberrations may be expected to impact the optical performance of typical OAPM systems at 1 THz and higher frequencies;
2. an OAPM pair should have (a, a) orientation to minimise aberrations at the focus;
3. if an (a, b) orientation is imposed by some other experimental constraint, then it will have aberrations in its image plane;
4. these aberrations can be inverted by a (b, a) pair.

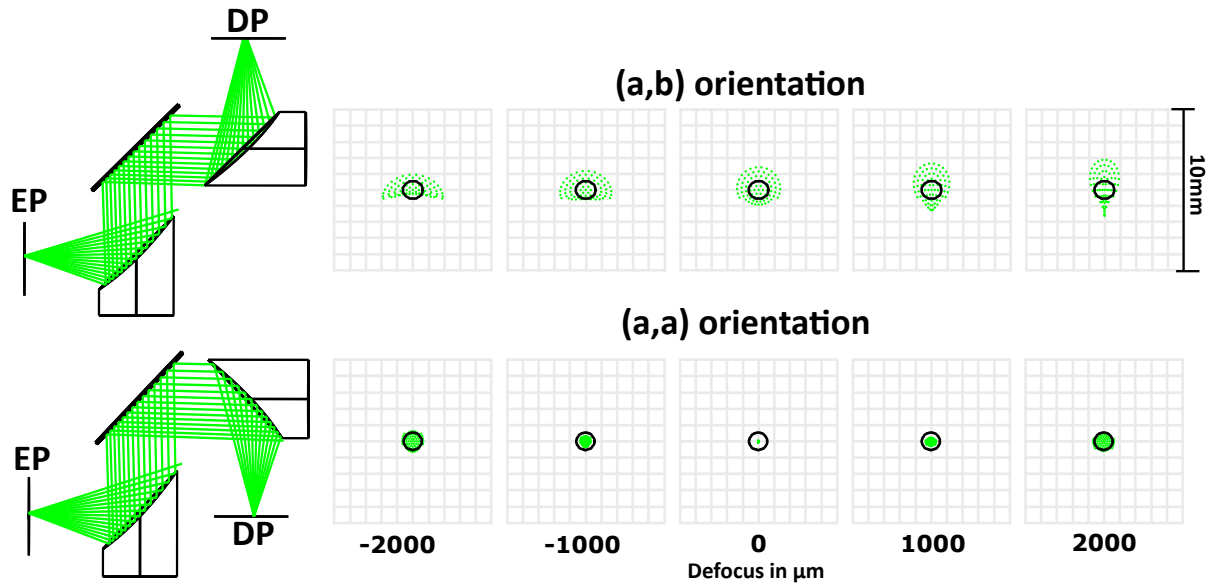


Fig. 6: Two OAPM geometry including a folding mirror, for a $(0,2)$ point source. Top row: (a,b) orientation (left) and through-focus spot diagrams (right). Bottom row: as first row, but for the (a,a) orientation of the second OAPM.

These rules allow the optimum OAPM orientation to be deduced for more complex spectrometer designs, without needing to ray-trace the geometry. For example, if an additional optic such as a mirror is required to change the THz beam direction, or to couple an optical beam along the optical axes of the OAPMs (using a THz mirror that passes visible light and reflects THz radiation), then it is desirable to know the optimum orientation for the OAPM(s) after the THz mirror. We now consider the setup pictured in Fig. 6, where a mirror is placed after the first OAPM, and the THz beam propagates along z . To form a focus, two orientations of the second OAPM are possible (top and bottom left diagrams). To identify the correct orientation of the final OAPM, such that aberrations are minimised, marginal ray notation and the rules above are useful. According to these rules the (a,a) configuration (bottom left) should be used as it will have less significant geometric aberrations than the (a,b) configuration (top left). Indeed the spot diagrams in the DP (right hand panels) validate this assertion. Similar considerations can be applied to correctly orient OAPMs in reflection geometry systems, where the THz beam reflected from a sample is collected, and THz beamsplitters are used.

Finally, it is worth discussing the impact of geometric aberrations on polarisation. There have been studies that reported asymmetric field and polarization distributions for OAPMs with different f -numbers used in the U- and step-shape [20]. Conversely, abrupt changes in THz polarization states were experimentally observed by Takai *et al.* [21], and were ascribed to the inherent geometry of the OAPMs. In the present study, the polarization performance of different OAPM geometries was not considered. We note that in a recent experimental study using multi-pixel THz emitters producing radial and azimuthal polarization, the polarization state can be experimentally corrected [22].

5 Conclusion

The study presented here contributes to a better understanding of the propagation and behaviour of THz pulses in multi-OAPM geometries. We demonstrated that geometric aberrations can limit the optical performance both in the sample and detector plane: they decrease the overall amplitude of the THz field and increase the spot size. Depending on the specific orientation of each OAPM in the optical system, the wavefront distortions, and aberrations at each subsequent focus, can be reduced or enhanced. We introduced marginal ray notation to capture the orientation of each OAPM in a system. The S-shape cancels out the geometric aberrations by the correct orientation of the second OAPM for each pair throughout the optical path, while the step-shape achieves good performance for off-axis rays at the detection plane, by the second pair of OAPMs cancelling out the distortion produced by the first pair. The use of the U-shape design should be discouraged as it adds, rather than subtracts, the distortion from each OAPM pair. Our modelling approach and design rules can be readily applied to the design of more complex THz imaging and spectroscopy setups based on OAPMs.

Declarations

Ethical Approval. N/A

Competing interests. The authors declare that they have no competing interests.

Authors' contributions. N.C. performed the optical modelling, prepared the figures, and drafted and edited the paper. J.L. drafted and edited the paper.

Funding. The authors would like to acknowledge funding from the EPSRC (UK) (Grant No. EP/V047914/1).

Availability of data and materials. ZEMAX modelling files and data are available from the authors on reasonable request.

References

1. C.D.W. Mosley, M. Failla, D. Prabhakaran, and J. Lloyd-Hughes. Terahertz spectroscopy of anisotropic materials using beams with rotatable polarization. *Scientific Reports*, 7(1):12337, 2017.
2. R. Rouzegar, A.L. Chekhov, Y. Behovits, B.R. Serrano, M.A. Syskaki, C.H. Lambert, D. Engel, U. Martens, M. Münzenberg, M. Wolf, G. Jakob, M. Kläui, T.S. Seifert, and T. Kampfrath. Broadband spintronic terahertz source with peak electric fields exceeding 1.5 MV/cm. *Phys. Rev. Appl.*, 19:034018, Mar 2023.
3. N. Chopra, J. Deveikis, and J. Lloyd-Hughes. Active THz beam shaping using a one-dimensional array of photoconductive emitters. *Applied Physics Letters*, 122(6):061102, 02 2023.
4. Y.-S. Lee. *Principles of terahertz science and technology*, volume 170. Springer Science & Business Media, 2009.
5. Q. Sun, X. Liu, J. Cao, R.I. Stantchev, Y. Zhou, X. Chen, E.P.J. Parrott, J. Lloyd-Hughes, N. Zhao, and E. Pickwell-Macpherson. Highly sensitive terahertz thin film total internal reflection spectroscopy reveals in situ photoinduced structural changes in methylammonium lead halide perovskites. *Journal of Physical Chemistry C*, 2018.
6. K. Reimann, M. Woerner, and T. Elsaesser. Two-dimensional terahertz spectroscopy of condensed-phase molecular systems. *Journal of Chemical Physics*, 154:120901, 3 2021.
7. R. Ulbricht, E. Hendry, J. Shan, T.F. Heinz, and M. Bonn. Carrier dynamics in semiconductors studied with time-resolved terahertz spectroscopy. *Reviews of Modern Physics*, 83:543, 6 2011.
8. J. Lloyd-Hughes, P. M. Oppeneer, T. Pereira Dos Santos, A. Schleife, S. Meng, M. A. Sentef, M. Ruggenthaler, A. Rubio, I. Radu, M. Murnane, X. Shi, H. Kapteyn, B. Stadtmüller, K. M. Dani, F. H. Da Jornada, E. Prinz, M. Aeschlimann, R. L. Milot, M. Burdanova, J. Boland, T. Cocker, and F. Hegmann. The 2021 ultrafast spectroscopic probes of condensed matter roadmap. *Journal of Physics: Condensed Matter*, 33:353001, 7 2021.
9. S.P.P. Jones, S.M. Gaw, K.I. Doig, D. Prabhakaran, E.M. Hétyroy Wheeler, A.T. Boothroyd, and J. Lloyd-Hughes. High-temperature electromagnons in the magnetically induced multiferroic cupric oxide driven by intersublattice exchange. *Nature Communications*, 5, 2014.
10. J. Lloyd-Hughes, G. Scalari, A. Van Kolck, M. Fischer, M. Beck, and J. Faist. Coupling terahertz radiation between sub-wavelength metal-metal waveguides and free space using monolithically integrated horn antennae. *Optics Express*, 17(20):18387 – 18393, 2009.
11. J. L. Tomaino, A. D. Jameson, J. W. Kevek, M. J. Paul, A. M. van der Zande, R. A. Barton, P. L. McEuen, E. D. Minot, and Y.-S. Lee. Terahertz imaging and spectroscopy of large-area single-layer graphene. *Opt. Express*, 19(1):141–146, Jan 2011.
12. E. Butler-Caddle, N.E. Grant, S.L. Pain, J.D. Murphy, K.D.G.I. Jayawardena, and J. Lloyd-Hughes. Terahertz photoconductance dynamics of semiconductors from sub-nanosecond to millisecond timescales. *Applied Physics Letters*, 122:012101, 1 2023.
13. A. Gürtler, C. Winnewisser, H. Helm, and P.U. Jepsen. Terahertz pulse propagation in the near field and the far field. *J. Opt. Soc. Am. A*, 17(1):74–83, Jan 2000.
14. Z. Jiang and X.-C. Zhang. 2D measurement and spatio-temporal coupling of few-cycle THz pulses. *Opt. Express*, 5(11):243–248, Nov 1999.
15. K.-E. Peiponen, A. Zeidler, and M. Kuwata-Gonokami. *Terahertz spectroscopy and imaging*, volume 171. Springer, 2012.
16. J. A. Murphy. Distortion of a simple gaussian beam on reflection from off-axis ellipsoidal mirrors. *International Journal of Infrared and Millimeter Waves*, 8:1165–1187, 9 1987.
17. P. Arguijo and M.S. Scholl. Exact ray-trace beam for an off-axis paraboloid surface. *Applied Optics*, Vol. 42, Issue 16, pp. 3284-3289, 42:3284–3289, 6 2003.
18. C. Brückner, G. Notni, and A. Tünnermann. Optimal arrangement of 90° off-axis parabolic mirrors in thz setups. *Optik*, 121(1):113–119, 2010.
19. N.J. Laurita, B. Cheng, R. Barkhouser, V.A. Neumann, and N.P. Armitage. A modified 8f geometry with reduced optical aberrations for improved time domain terahertz spectroscopy. *Journal of Infrared, Millimeter, and Terahertz Waves*, 37:894–902, 2016.
20. S. Sung, J. Garritano, N. Bajwa, B. Nowroozi, W. Grundfest, and Z. Taylor. Analysis and optimization of THz imaging optics with off-axis parabolic mirrors. In *2014 39th International Conference on Infrared, Millimeter, and Terahertz waves (IRMMW-THz)*, pages 1–2, 2014.
21. M. Takai, K. Shibata, M. Uemoto, and S. Watanabe. Spatial polarization variation in terahertz electromagnetic wave focused by off-axis parabolic mirror. *Applied Physics Express*, 9(5):052206, 2016.
22. J. Deveikis and J. Lloyd-Hughes. Multi-pixel photoconductive emitters for the controllable generation of azimuthal and radial terahertz beams. *Optics Express*, 30:43293–43300, 11 2022.